Scaled Test Program Strategy of Skin Heat Exchanger for Thermal Management in Hybrid Electric Regional Aircraft

Benigno J. Lázaro * and Ezequiel González-Martínez

Posted Date: 3 March 2026

doi: 10.20944/preprints202603.0239.v1

Keywords: skin heat exchanger;hybrid electric propulsion regional aircraft;scaled wind tunnel tests;CFD

 doi:10.20944/preprints202603.0239.v1

Article

Scaled Test Program Strategy of Skin Heat Exchanger for Thermal Management in Hybrid Electric Regional Aircraft

Benigno J. Lázaro * and Ezequiel González-Martínez

Department of Aerospace Fluid Mechanics and Propulsion, Universidad Politécnica de Madrid

* Correspondence: benigno.lazaro@upm.es

Abstract

The strategy developed to carry out a scaled test program aimed at reproducing the behavior of skin heat exchangers to alleviate the heat dissipation requirements in future hybrid electric propulsion regional aircraft is presented. The test program is intended to reproduce, as best possible, the conditions faced by the skin heat exchanger on a predefined nominal cruise flight operation, while conducting the tests in a wind tunnel operating at low velocities and near standard atmospheric conditions. For that purpose, dimensional analysis is used to establish the best geometrical scale and approach flow conditions in the wind tunnel test program. The validation of the strategy is achieved by comparing dimensionless parameters characterizing the turbulent heat transfer process taking place at the skin heat exchanger/airflow interface surface in the flight and wind tunnel environments, by using CFD analysis based on RANS turbulence modeling. The comparison reveals that the adopted wind tunnel strategy is indeed capable of reproducing the heat transfer process taking place in the flight environment, thus paving the way to achieve mid TLR validation of the skin heat exchanger technology.

Keywords: skin heat exchanger; hybrid electric propulsion regional aircraft; scaled wind tunnel tests; CFD

1. Introduction

Regional aircrafts based on hybrid electric propulsion (HERA) are one of the key elements to reduce carbon emissions in the short and medium range aircraft operation, having in mind the ambitious objective set in the Strategic Research and Innovation Agenda (SRIA) [1], which entails a 50% emission reduction in Green House Gas (GHG) with respect to current state of the art technology for HERA. Conceptual studies indicate that hybrid electric propulsion leads to heavier aircraft than the thermal ones, and HERA only makes sense in a scenario of cutting CO2 emissions [2]. Different ongoing HERA projects are already being developed, aiming at having platform airworthiness by the late-2020s for small 20 seats concepts and by the mid-2030s for 50-100 seats and distances less than 500 km. For this latter application, HERA should include hybrid-electric propulsion based on batteries or fuel cells as energy sources, supported by SAF or hydrogen burning for the thermal source, to reach up to 90% lower emissions while being fully compliant with International Civil Aviation Organization (ICAO) noise rules.

To be successful, HERA development will need to integrate disruptive enable technologies including high voltage MW scale electrical distribution, new hybrid-electric propulsion and related new energy storage at low GHG generation, and high-capacity thermal management. Regarding this aspect, HERA will have to face very demanding on-board thermal management issues, as heat dissipation requirements in these aircrafts are expected to undergo order of magnitude increases with respect to current needs, typically escalating from 50 kW levels to close to 1 MW figures. As a result,

 doi:10.20944/preprints202603.0239.v1

advanced compact, lightweight, and highly efficient heat dissipation concepts will need to be developed in order to meet the stringent heat management requirements attached to HERA.

One of the concepts being investigated is the skin heat exchanger (SHX), which uses the skin of the aircraft and the airflow sweeping over it as the heat sink process. To meet the high heat dissipation capacity and compact architecture demanded by highly efficient HERA designs, SHX systems will need to incorporate phase change in the aircraft bound cooling circuit. Reviews of conceptual designs for thermal management in HERA [3,4] indicate that SHX combined with a gas/liquid cooling circuit including phase change could offer significant benefits, minimizing drag penalties induced by alternative ram air driven heat exchangers. Furthermore, conceptual design studies point out that ram air could not address alone the high-demanding heat dissipation required by HERA without incurring in unacceptable penalties on aircraft aerodynamics [5,6]. However, in order to complement or to be a meaningful alternative to conventional heat drain concepts, SHX technology must demonstrate high enough heat exchange fluxes to offset its weight and size penalties.

A potential hurdle for the integration of SHX technology in HERA could be the introduction of composite materials in aircraft structures [7], which have proved to reduce fuel consumption by 12% in the last generation of aircrafts but which could limit efficient heat transfer from the aircraft skin [3], though additive manufacturing with metals [7] or aluminum skin could offer a good trade-off solution for SHX heat dissipation surfaces. A more detailed conceptual study on the impact of SHX on aircraft aerodynamics [8] postulates that friction drag decreases on turbulent boundary layers acting as SHX heat sinks, even though the study considered simple heat transfer coefficients based on flat plate correlations [9–12]. Further assessment of the SHX potential aerodynamic performance on lifting surfaces has been conducted with the help of CFD studies [13–16] incorporating RANS turbulent models [17,18], where the ability of CFD simulations to track heat transfer and aerodynamic coefficients was validated against experimental data of icing devices on wing profiles [19] with some degree of success. The optimal position of SHX installed on the lifting surfaces seems to be at the pressure side [13,14], where a smaller impact on the aerodynamic performances is expected. However, heating both the suction and pressure sides of the wing [15,16] could degrade aerodynamic efficiency by up to 15% at high surface temperatures [15], due to the negative impact on the suction side of the aerodynamic profiles. Furthermore, heat transfer delivered by SHX could be compromised at low velocities and high power-demanding regimes, such as take-off or climbing [13,14]. These flight regimes could require a temporally back-up heat sink process like one based on the fuel delivery system, or else SHX could take advantage of the high-speed slipstream from the propellers [15]. An alternative to lifting surface installation of SHX is the sponsons surfaces for the landing gear, offering a close to zero pressure gradient (ZPG) environment which could reduce friction drag and allow an efficient installation of the SHX hardware.

Conceptual studies for the selection of the working fluid in the coolant circuit of SHX have placed the focus on the family of HFO coolants [20,21] with change of phase models [21,22], which are categorized as ozone-friendly, low global warming potential. Semi-empirical correlations for heat transfer coefficients on pipes and flat plates has demonstrated that HFO-1234yf, 1233zd exhibit a great potential for reducing the size of the SHX surface. With regards to the relative coolant and airflow directions, semi-empirical procedures [21,23] concluded that parallel co-flows demonstrate superior mechanical and heat transfer performances than counter-flow configurations. Finally, cooling conduits of square cross-section seem to be the optimal choice for the coolant duct [20,21,23,24], based on a compromise between optimizing heat transfer and pressure drop coefficients with minimum weight and size penalties.

Increasing the SHX TRL level beyond conceptual studies calls for preliminary, dedicated experimental validation programs that can reproduce the main features of the SHX operation in nominal flight operation. This implies an external to aircraft airflow characterized by ~0.5 Mach numbers with nominal flight pressure and temperature levels. In addition, the boundary layer of the airflow sweeping over the SHX airflow exposed surface should be turbulent with realistic boundary layer scales. Performing the early SHX development tests while matching all these airflow conditions

 doi:10.20944/preprints202603.0239.v1

is not feasible using wind tunnels operating near standard atmospheric conditions. As a result, it is necessary to develop a test strategy to reproduce the SHX operation to be found in the nominal flight conditions while using standard, atmospheric wind tunnel test benches. The aim of this work is to develop such strategy for setting a wind tunnel test environment that would best establish physical similarity with the results achieved by SHX under nominal HERA flight conditions, by using a low-speed wind tunnel operating at near standard atmospheric conditions as the SHX external airflow generation system.

2. SHX Airflow Modeling

In SHX architectures, either the fuselage or the lifting surfaces can be used as surfaces to dissipate heat to the airflow sweeping the aircraft. For HERA architectures, although lifting surfaces can be considered as potential installation sites, aerodynamic performance issues indicate that the sponsons used as fairing for the aft landing gear could be the optimal choice to base the SHX airflow exposed surfaces [13–15]. This option has many advantages, as it allows locating the SHX elements away from the cabin to minimize SHX integration problems while benefiting both from relatively thin yet turbulent boundary layer development to augment the heat transfer coefficient and providing enough surface to achieve heat dissipation levels of the order of 100 kW. Figure 1 shows the sponson installation zone to locate the airflow exposed SHX surface in a conceptual HERA design. With this arrangement, the expected available SHX heat dissipation area would be of the order of $10\,m^2$ per sponson, and the leading edge of the SHX airflow exposed surface could be located at distances from the sponson leading edge of the order of $1\,m$, thus ensuring a turbulent yet thin boundary layer sweeping over the SHX airflow exposed surface.

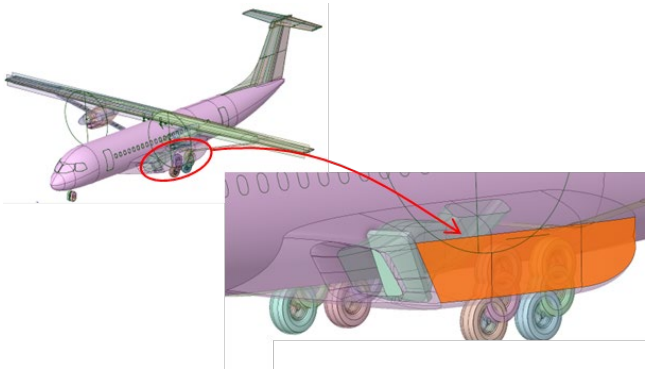

Figure 1. HERA concept and airflow exposed SHX surface using the sponson location as SHX installation site.

A SHX conceptual basic geometry is shown in Figure 2. The cooling fluid flows over several parallel cooling channels which are also exposed to the aircraft exterior airflow through the sponson wall. For the schematic design shown in Figure 2, each cooling channel exhibits a rectangular cross section as previous studies [20,21,23,24] indicate that it could offer benefits to maximize the heat transfer from the cooling fluid. To ensure high heat fluxes and thus a compact layout, the SHX operates the cooling fluid allowing phase change in the cooling channels. Thus, the cooling fluid enters the SHX cooling channels as a slightly superheated vapor with a liquid mass fraction $\chi_{ci} \approx 0$ and leaves it as a slightly subcooled liquid with $\chi_{ci} \approx 1$. Figure 2 also shows the coordinate system used to describe the SHX/airflow heat transfer, having its origin on the SHX wall exposed to the airflow and at the streamwise location where the leading edge of the SHX is placed, with the x axis running parallel to the external airflow streamwise direction and the y axis being normal to the SHX wall exposed to the airflow and pointed towards the latter.

 doi:10.20944/preprints202603.0239.v1

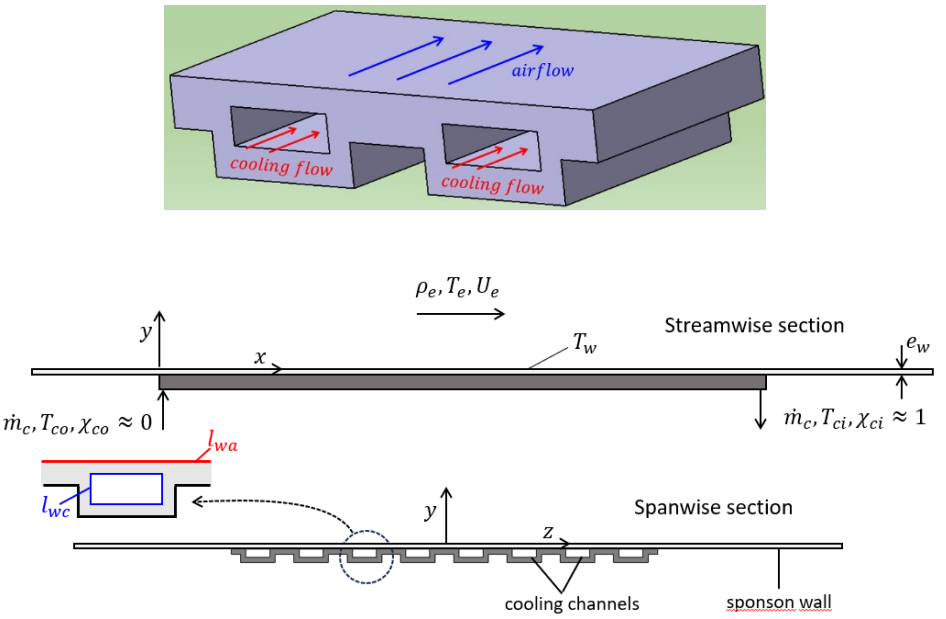

Figure 2. SHX schematic view, showing a segment of the SHX and streamwise and spanwise sections with cooling channel detail.

The sponson wall is represented in Figure 2 as the surface denoted with wall thickness e_w. Each cooling channel has effective heat exchange perimeters in contact with the cooling fluid and with the external airflow respectively denoted as l_{wc}, l_{wa}, with $l_{wc}/l_{wa} = O(1)$. Except for local spanwise end effects, each cooling channel can be considered to operate under periodic spanwise conditions. Table 1 summarizes the main nominal flight operating parameters, with subscripts e, c respectively denoting SHX exterior airflow and cooling channel fluid conditions. The exterior airflow corresponds to HERA operating in nominal cruise at ISA flight level FL250 and Mach number $M_e \approx 0.50$. A nominal design with characteristic distance of $\sim 1.5\, m$ between the sponson leading edge and the SHX leading edge is considered to provide space to accommodate the different hardware components included in the SHX system with minimum aerodynamic penalty.

Table 1. SHX main operating parameters at nominal flight conditions.

$p_e\ (kPa)$	$T_e\ (K)$	$u_e (m/s)$	$\Delta x_{le}\ (m)$ [1]	$T_c\ (K)$	$p_c\ (kPa)$	$q_{ce}\ (kW/m^2)$
37.6	239	~ 150	~ 1.5	~ 323	~ 300	> 5

[1] Streamwise distance between sponson and SHX leading edges.

The requirement set in Table 1 for the SHX dissipated heat flux q_{ce} implies that considering two independent SHX units with characteristic surface each of $10\, m^2$ a total heat dissipation of at least $100\, kW$ can be achieved.

As a result of the phase change, the SHX cooling channel operates almost at isobaric and isothermal conditions. Thus, the temperature in the SHX solid wall in contact with the cooling fluid can be considered to take a uniform value T_c in all its length, corresponding to the cooling fluid condensation temperature at pressure p_c. In addition, the airflow established over the sponson surface can be considered to develop as a zero-pressure gradient (ZPG) turbulent boundary layer, as schematically depicted in Figure 3.

 doi:10.20944/preprints202603.0239.v1

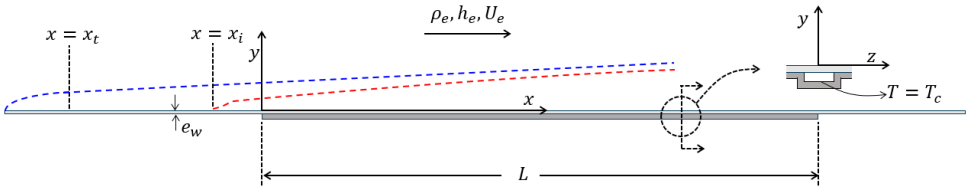

Figure 3. Airflow momentum (broken blue line) and thermal (broken red line) boundary layers developing over the sponson and SHX surfaces exposed to the airflow.

The SHX spans the streamwise coordinates $0 \leq x \leq L$. As stated above, a uniform temperature boundary condition T_c can be prescribed at the SHX solid wall limiting the fluid cooling channels. For the solid SHX and sponson walls not exposed to the airflow or to the cooling fluid an adiabatic boundary condition can be approximately prescribed. The momentum boundary layer of the airflow will have its origin at the leading edge of the sponson. Shorty after it, the boundary layer will undergo transition to turbulence at a downstream location denoted as $x_t < 0$ in Figure 3. As a result of heat conduction taking place through the sponson wall, the airflow thermal boundary layer will be initiated upstream of the SHX, at a location denoted as $x_i < 0$ in Figure 3. Likewise, some heat exchange to the airflow will also take place downstream from the SHX, at locations verifying $x > L$. Considering the streamwise segment $0 \leq x \leq L$ covered by the SHX, an estimate of the solid wall temperature T_{wa} exposed to the airflow can be given after establishing the balance between the heat exchanged between the SHX solid wall on both its airflow and cooling fluid interfaces:

$$k_w \frac{T_c - T_{wa}}{e_w} l_{wc} \approx Sta_c \rho_e U_e c_p (T_{wa} - T_e) l_{wa} , \tag{1}$$

with $Sta_c = O(10^{-3})$ being a characteristic value of the Stanton number for the SHX-airflow heat exchange process, and with k_w denoting the heat conductivity of the solid SHX/sponson wall. Expression (1) can be rearranged to give:

$$0 \leq x \leq L: \; T_{wa} \approx \frac{T_c + \epsilon_{wa} T_e}{1 + \epsilon_{wa}}, \epsilon_{wa} \approx \frac{Sta \rho_e U_e c_p e_w}{k_w} \frac{l_{wa}}{l_{wc}} = O(10^{-2}) \; \rightarrow \; T_{wa} \approx T_c \tag{2}$$

The estimate given in (2) for ϵ_{wa} follows after considering values presented in Table 1 and SHX solid wall parameters $e_w = O(10^{-3} m)$, $k_w = O(10^2 \, W/mK)$, $l_{wa}/l_{wc} = O(1)$.

The first important implication of estimate (2) is that, except for local spanwise end effects, the spanwise modulation of the airflow magnitudes should be weak and thus the airflow boundary layer should be almost two-dimensional. This suggests defining airflow magnitudes that are averaged along the spanwise direction z, in a spanwise interval equal to half the spanwise separation between consecutive cooling channels. In what follows it will be assumed that airflow magnitudes have been spanwise averaged in this fashion.

A second important implication of (2) is that, considering values given in Table 1, we can write for the airflow:

$$0 \leq x \leq L: \qquad \frac{\Delta T_{y,T_c}}{T_e} \approx \frac{T_c - T_e}{T_e} \tag{3}$$

with $\Delta T_{y,T_c}$ being the temperature difference taking place across the airflow boundary layer. The airflow boundary layer also heats up from the combined action of compressibility effects and of the reduced velocities taking place near the solid wall. Denoting $\Delta T_{y,M_e}$ as the airflow temperate increment due to this effect, and according to the flight operation values given in Table 1, it follows:

$$\frac{\Delta T_{y,M_e}}{\Delta T_{y,T_c}} \sim \frac{(\gamma - 1) M_e^2}{2(T_c/T_e - 1)} = O(10^{-1}) \tag{4}$$

 doi:10.20944/preprints202603.0239.v1

Expression (4) indicates that the airflow temperature increase resulting from the flight Mach number and viscous heating is an order of magnitude smaller than the one established by the SHX operation. Thus, the equations describing the development of the airflow boundary layer can be approximated in a first instance by considering the limit $M_e^2 \to 0$, with airflow compressibility effects only showing through the heating of the solid wall by the SHX cooling flow. For the laminar case it is possible to define a change of variables such as the Stewartson transformation [12] that will define an equivalent incompressible boundary layer to account for non-negligible Mach number effects. However, such transformations are based on simplifications taken for the molecular transport terms that cannot be applied to the turbulent boundary layer because of its multiscale character and the difficulty to properly handle the turbulent stresses and energy fluxes. Thus, and considering (4), the limit $M_e^2 \to 0$ will be considered for the equations governing the mean airflow boundary layer and the solid wall temperature, which in that case can be written as:

$$\frac{\partial(\bar{\rho}\tilde{u})}{\partial x} + \frac{\partial(\bar{\rho}\tilde{v})}{\partial y} = 0 \tag{5.1}$$

$$\bar{\rho}\tilde{u}\frac{\partial \tilde{u}}{\partial x} + \bar{\rho}\tilde{v}\frac{\partial \tilde{u}}{\partial y} = \frac{\partial}{\partial y}\left(\left(\mu(\tilde{T}) + \mu_t\right)\frac{\partial \tilde{u}}{\partial y}\right) \tag{5.2}$$

$$\bar{\rho}\tilde{u}\frac{\partial \tilde{h}}{\partial x} + \bar{\rho}\tilde{v}\frac{\partial \tilde{h}}{\partial y} = \frac{\partial}{\partial y}\left(\left(\frac{\mu(\tilde{T})}{Pr} + \frac{\mu_t}{Pr_t}\right)\frac{\partial \tilde{h}}{\partial y}\right) \tag{5.3}$$

$$\frac{\partial^2 T_w}{\partial x^2} + \frac{\partial^2 T_w}{\partial y^2} + \frac{\partial^2 T_w}{\partial z^2} = 0 \tag{5.4}$$

In these expressions $\tilde{(\,)}$ and $\bar{(\,)}$ respectively denote Favre and time averaged magnitudes. The thermodynamics closure for the above equations can be expressed as:

$$\bar{\rho} \approx \rho_e\left(\frac{\tilde{h}}{h_e}\right)^{-1};\ \mu(\tilde{T}) \approx \mu(T_c)\left(\frac{\tilde{T}}{T_c}\right)^{n} = \mu(T_c)\left(\frac{T_c}{T_e}\right)^{-n}\left(\frac{\tilde{h}}{h_e}\right)^{n}, n \approx 0.7 \tag{6}$$

The simplified viscosity law introduced in (6) is very accurate for temperatures close to T_c [25]. As viscous effects for the system of equations (5) are only significant in the turbulent wall layer, characterized by temperatures close to T_c, the simplified viscosity law (7) should be very representative.

A turbulent closure for equations (5.2)-(5.3) can be proposed by introducing two scales characterizing the development of the turbulent boundary layer, namely the wall friction velocity $u_\tau(x)$ and the global thickness given by the Rotta-Clauser length scale $\Delta(x)$ [26], which are defined as:

$$u_\tau(x) = \sqrt{\left(\frac{\mu(\tilde{T})}{\bar{\rho}}\frac{\partial \tilde{u}}{\partial y}\right)_{y=0}} = \sqrt{\frac{\mu(T_c)}{\rho_e}\left(\frac{T_c}{T_e}\right)^{-n}\left(\left(\frac{\tilde{h}}{h_e}\right)^{n+1}\frac{\partial \tilde{u}}{\partial y}\right)_{y=0}} \tag{7.1}$$

$$\Delta(x) = \left(\frac{u_\tau(x)}{U_e}\right)^{-1}\int_0^\infty\left(1 - \frac{\bar{\rho}\tilde{u}}{U_e\rho_e}\right)dy \tag{7.2}$$

With these two scales, a local model for the turbulent viscosity μ_t can be proposed [27] to give:

$$\frac{\mu_t}{\bar{\rho}\Delta u_\tau} \approx g\left(\frac{y}{\Delta}, \frac{\bar{\rho}\Delta u_\tau}{\mu(\tilde{h})}\right) \tag{7.3}$$

The system (5)-(7) must be complemented with appropriate boundary conditions. If the airflow inlet is defined at a location x_i sufficiently upstream from the SHX, the airflow boundary conditions become:

 doi:10.20944/preprints202603.0239.v1

$$y = 0: \qquad \tilde{u} = 0, \;\; \tilde{v} = 0 \tag{8.1}$$

$$y \to \infty: \qquad \tilde{u} \to U_e, \;\; \tilde{h} \to h_e, \;\; \bar{\rho} \to \rho_e \tag{8.2}$$

$$x = x_i: \qquad u_\tau = u_{\tau i}; \;\; \Delta = \Delta_i; \;\; \frac{\tilde{u}}{U_e} = f_i\left(\frac{y}{\Delta_i}, \frac{u_{\tau i}}{U_e}\right); \;\; \frac{\tilde{h}}{h_e} \approx 1; \;\; \frac{\bar{\rho}}{\rho_e} \approx 1 \tag{8.3}$$

with f_i denoting the dimensionless velocity profile of the ZPG, adiabatic turbulent boundary layer.

The surfaces defining the boundaries of the solid wall (Figure 4) can be classified as the solid wall-airflow boundary, Σ_{wa}; the solid wall-cooling channel boundary, Σ_{wc}; and the solid wall not in contact with either the external airflow or the cooling fluid, Σ_{w0}. If the geometry of the cooling fluid channel and the inter-channel separation are of the order of the sponson wall thickness e_w, surfaces Σ_{wc}, Σ_{w0} introduce two characteristic lengths: the SHX streamwise length L, and the sponson wall thickness e_w. Boundary conditions at the solid wall boundary not in contact with the airflow can then be specified as:

$$\Sigma_{wc}, \;\; f_{wc}(x, y, z, e_w, L) = 0: \quad T_w = T_c = \frac{T_c}{T_e} T_e \tag{8.4}$$

$$\Sigma_{w0}, \;\; f_{w0}(x, y, z, e_w, L) = 0: \quad \nabla T_w \cdot \nabla f_{w0} = 0 \tag{8.5}$$

In addition, the compatibility of temperature and heat flux must be imposed at the solid wall/airflow interface surface Σ_{wa}:

$$\Sigma_{wa}, \;\; y = 0: \quad \tilde{h} = c_p T_w; \;\; \frac{\mu(T_c)}{Pr k_w}\left(\frac{T_c}{T_e}\right)^{-n}\left(\frac{\tilde{h}}{h_e}\right)^{n}\frac{\partial \tilde{h}}{\partial y} = \frac{\partial T_w}{\partial y} \tag{8.6}$$

Upstream and downstream of the SHX, equation (5.4) can be integrated along the $y-z$ directions to give a one-dimensional equation for the streamwise evolution of the cross-stream averaged sponson wall temperature T_{wx}:

$$x < 0; \; x > L \; : \qquad k_w e_w \frac{d^2 T_{wx}}{dx^2} \approx Sta_c \rho_e U_e \left(c_p T_{wx} - h_e\right) \tag{9}$$

with $Sta_c = O(10^{-3})$ again representing a characteristic value of the Stanton number for the SHX/airflow heat transfer. Equation (9) defines a characteristic length x_w that sets the scale for the length upstream and downstream from the SHX where the cross-stream averaged sponson wall temperature T_{wx} relaxes to the value T_e imposed by the external flow:

$$x_w \approx \sqrt{\frac{k_w e_w}{Sta_c \rho_e U_e c_p}} \tag{10}$$

At streamwise locations $x \approx -5x_w$ the sponson wall temperature should approach the exterior airflow temperature. Thus, this location can be selected to specify, using expressions (8.3), the state of the adiabatic, ZPG turbulent boundary layer approaching the SHX:

$$x_i \approx -150 \sqrt{\frac{k_w e_w}{\rho_e U_e c_p}} \tag{11}$$

Dimensional analysis of the system (5)-(7) with boundary conditions (8) and definition (11) allows writing the following generic dependence for the unknowns:

$$\begin{pmatrix} \bar{\rho} \\ \tilde{u} \\ \tilde{v} \\ \tilde{h} \\ T_w \end{pmatrix} = \begin{pmatrix} \bar{\rho} \\ \tilde{u} \\ \tilde{v} \\ \tilde{h} \\ T_w \end{pmatrix} \left\{ x, y, Pr, Pr_t, \mu(T_c), n, \frac{T_c}{T_e}, U_e, \rho_e, h_e, \Delta_i, u_{\tau i}, e_w, L, x_i, k_w \right\} \tag{12}$$

 doi:10.20944/preprints202603.0239.v1

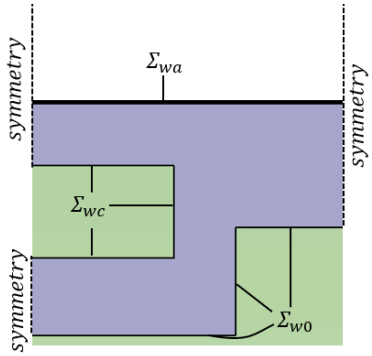

Figure 4. Schematic view of surfaces defining the boundaries of the SHX solid wall.

The dimensionless formulation of the airflow/SHX solid wall problem can be achieved by selecting an appropriate set of parameters. Specifically, exterior airflow magnitudes and the boundary layer thickness at $x = x_i$ can be used for that purpose:

$$(U_e, \rho_e, h_e, \Delta_i) \tag{13}$$

Using these magnitudes as the set to render a dimensionless expression of the airflow/SHX solid wall problem, leads to the definition of the following dimensionless variables:

$$\hat{x} = \frac{x}{\Delta_i};\ \hat{y} = \frac{y}{\Delta_i};\ \hat{z} = \frac{z}{\Delta_i};\ \hat{\rho} = \frac{\bar{\rho}}{\rho_e};\ \hat{u} = \frac{\tilde{u}}{U_e};\ \hat{v} = \frac{\tilde{v}}{U_e};\ \hat{h} = \frac{\tilde{h}}{h_e};\ \hat{T}_w = \frac{T_w}{T_e} = \frac{c_p T_w}{h_e};$$
$$\hat{u}_\tau = \frac{u_\tau}{U_e};\ \hat{\Delta} = \frac{\Delta}{\Delta_i};\ \hat{\mu}_t = \frac{\mu_t}{\rho_e \Delta_i U_e} \tag{14}$$

The additional dimensional parameters that appear in (12) generate a number of controlling dimensionless parameters. Specifically:

$$Re = \frac{\rho_e U_e \Delta_i}{\mu(T_c)};\quad \hat{T}_c = \frac{T_c}{T_e};\quad \hat{u}_{\tau i} = \frac{u_{\tau i}}{U_e};\quad \hat{L} = \frac{L}{\Delta_i};\quad \hat{e}_w = \frac{e_w}{\Delta_i}; \tag{15.1}$$

$$\hat{k}_w = \frac{k_w Pr}{c_p \mu(T_c)};\quad \hat{x}_i = \frac{x_i}{\Delta_i} \approx -150\sqrt{\frac{\hat{k}_w \hat{e}_w}{PrRe}} \tag{15.2}$$

The parameter $\hat{k}_w$ appears when writing the dimensionless expression of the temperature and heat flux continuity condition (8.6) at the sponson wall/airflow interface surface:

$$\hat{\Sigma}_{wa},\ \hat{y} = 0{:}\quad \hat{h} = \hat{T}_w,\ \hat{k}_w^{-1}\left(\frac{T_c}{T_e}\right)^{-n} \hat{h}^n \frac{\partial \hat{h}}{\partial \hat{y}} = \frac{\partial \hat{T}_w}{\partial \hat{y}} \tag{16}$$

The dimensionless parameters that appear in (15.1) and (15.2) have been classified according to their impact in the dimensionless formulation of the airflow/SHX solid wall heat transfer process. Thus, parameters Re and $\hat{T}_c$ control the development of the airflow boundary layer and thus they should be carefully matched in a scaled test program. Assuming that the exterior airflow conditions are given, matching these two parameters sets the appropriate scale for the thickness Δ_i of the boundary layer approaching the SHX. In turn, this value determines the geometrical scale of the wind tunnel tests, including the characteristic thickness e_w setting the sponson and SHX solid walls.

Matching the parameters that appear in (15.2) is less critical. In particular, the parameter $\hat{k}_w$ is just the ratio between the thermal conductivities of the SHX solid wall and of the airflow at temperature T_c. For the value of this temperature given in Table 1 and $k_w = O(10^2\ W/mK)$ it follows $\hat{k}_w = O(10^3)$. This very large order of magnitude ensures that the parameter ϵ_{wa} that appears in expression (2) remains small and that the temperature of the airflow/SHX solid wall interface surface becomes close to T_c. Thus, as long as $\hat{k}_w \gtrsim O(10^3)$ the specific value adopted by $\hat{k}_w$ should have a secondary effect in the airflow/SHX heat transfer process, only leading to small deviations in the

 doi:10.20944/preprints202603.0239.v1

dimensionless temperature and heat flux values for the airflow solution. Small discrepancies of $\hat{k}_w$ will have also a secondary impact in the specific value of the location $\hat{x}_i$ where to specify the initial conditions for the approaching turbulent boundary layer, as its impact is somewhat smoothed by the presence of the root square in definition (10).

Regarding the specification of the initial state for the airflow boundary layer at $x = x_i$, recall that the streamwise position x_t is defined as the location where the laminar to turbulent transition takes place over the sponson wall. Furthermore, since over the streamwise segment $x_t < x < x_i$ the turbulent boundary layer develops under adiabatic, equilibrium conditions it can be written:

$$x_t < x < x_i: \qquad \hat{u}_{\tau i} = \hat{u}_{\tau i}\left(\hat{T}_c^n Re\right) \tag{17}$$

Considering the above discussion, the dimensionless dependence of the airflow and of the SHX solid wall heat transfer problem can be written as:

$$\begin{pmatrix} \hat{u} \\ \hat{v} \\ \hat{h} \\ \hat{T}_w \end{pmatrix} = \begin{pmatrix} \hat{u} \\ \hat{v} \\ \hat{h} \\ \hat{T}_w \end{pmatrix} \left\{\hat{x}, \hat{y}; Re, \hat{T}_c, \hat{L}, \hat{x}_i, \hat{k}_w, Pr, Pr_t, n\right\}; \quad \hat{\rho} = \hat{h}^{-1} \tag{18}$$

The dimensionless friction velocity, boundary layer thickness, and turbulent viscosity become:

$$\hat{u}_\tau = \sqrt{\frac{1}{Re\hat{T}_c^n}\left(\hat{h}^{n+1}\frac{\partial \hat{u}}{\partial \hat{y}}\right)_{\hat{y}=0}}; \quad \hat{\Delta} = \frac{1}{\hat{u}_\tau}\int_0^\infty (1-\hat{\rho}\hat{u})d\hat{y}; \quad \hat{\mu}_t \approx \frac{\hat{\Delta}\hat{u}_\tau}{\hat{h}} g\left(\frac{\hat{y}}{\hat{\Delta}}, \hat{T}_c^n Re\frac{\hat{\Delta}\hat{u}_\tau}{\hat{h}^{(n+1)}}\right) \tag{19}$$

Expression (18) gives the dependence of the dimensionless airflow magnitudes and solid wall temperature, which allows proposing the appropriate scaling of wind tunnel tests conducted at near standard conditions to reproduce the heat transfer process taking place over the sponson wall in nominal flight operation. Considering that the parameters (Pr, Pr_t, n) are independent of the airflow operation conditions, the following constraints should be enforced to ensure physical similarity of the airflow/SHX heat transfer process between the wind tunnel scale tests and the nominal flight operation:

- Geometrical similarity
- Identical values of key dimensionless parameters, namely, $Re = \rho_e U_e \Delta_i/\mu(T_c)$, $\hat{T}_c = T_c/T_e$, $\hat{L} = L/\Delta_i$, $\hat{x}_i = x_i/\Delta_i$.
- Large enough value of the dimensionless parameter $\hat{k}_w$, $\hat{k}_w \gtrsim O(10^3)$.

With the conditions given in Table 1, only the initial value of the boundary layer thickness Δ_i needs to be specified at streamwise location x_i to fully define the magnitude set given in (14) for the nominal flight operation. The evolution of the boundary layer upstream of the SHX can be estimated by considering a characteristic distance separating the leading edges of the sponson and of the SHX, and that the sponson wall behaves as a flat plate. Selecting $x_{le} \approx -1.5\ m$ as a safe margin to install the SHX with minimum aerodynamic penalty, the evolution of the boundary layer over the sponson wall would include first a short laminar development followed by a transition process and a posterior turbulent development. The transition Reynolds number based on the distance from the sponson leading edge will depend on the free stream turbulence level and on the sponson's leading edge region geometry. Considering a characteristic transition Reynolds number based on the exterior airflow properties and on development distance $(x_t - x_{le})$ of the order of $2 \cdot 10^6$ [12], the location of transition for nominal flight operation verifies:

$$(x_t - x_{le}) \approx 2 \cdot 10^6 \frac{\mu(T_e)}{\rho_e U_e} \approx 0.40\ m \tag{20}$$

The evolution of the ZPG sponson boundary layer after transition can be estimated by considering the logarithmic friction law and von Karman's boundary layer equation [28]:

$$\frac{U_e}{u_\tau} \approx \frac{1}{\kappa}\ln\frac{\rho_e \Delta u_\tau}{\mu(T_e)} + 4.7 \tag{21.1}$$

 doi:10.20944/preprints202603.0239.v1

$$\frac{U_e}{u_\tau^2}\frac{d}{dx}(\Delta u_\tau) \approx 1 \qquad (21.2)$$

Rearranging these equations gives the evolution of the Reynolds number defined from the exterior airflow properties and development distance $(x - x_t)$ as a function of a Reynolds number $Re_{\Delta\tau}$ constructed from the product Δu_τ:

$$\frac{\rho_e (x - x_t) U_e}{\mu(T_e)} \approx \int \left(\frac{1}{\kappa}\ln Re_{\Delta\tau} + 4.7\right)^{-2} dRe_{\Delta\tau}, \quad Re_{\Delta\tau} = \frac{\rho_e \Delta u_\tau}{\mu(T_e)} \qquad (22)$$

The lower bound for the integral in (22) can be taken with a characteristic value at transition $Re_{\Delta\tau} \approx 10^3$, although for development distances verifying $(x - x_t) = O(1\,m)$ any value of this Reynolds number selected in the range $10^2 - 10^3$ will have negligible impact in the evolution of expression (22). Equations (21.1) and (22) then give the evolution of the two scales (Δ, u_τ) characterizing the turbulent boundary layer that develops over the sponson wall. These equations can be applied to determine these two scales at station x_i given in (11). For the nominal flight conditions, considering a sponson wall $e_w \approx 0.002\,m$ made of aluminum alloy with $k_w \approx 170\ W/mK$ it results:

$$x_i \approx -0.30\,m \qquad (23)$$

Solving equations (21.1) and (22) for $(x_i - x_t) \approx 0.8\,m$ leads to establishing the scales of the turbulent boundary layer at x_i for the nominal flight operation:

$$x = x_i: \qquad \Delta_i \approx 0.040\,m, \quad \frac{u_\tau}{U_e} \approx 0.038 \rightarrow \qquad \hat{x}_i = \frac{x_i}{\Delta_i} \approx -7.5 \qquad (24)$$

3. Wind Tunnel Scaled Tests Specification

The facility to carry out the SHX scaled tests (Figure 5) is an open return, suction type wind tunnel operating at near atmospheric conditions, with nominal free stream operating conditions of pressure, temperature and density respectively given by $p_e \approx 99.0\,kPa$, $T_e \approx 288\,K$, $\rho_e \approx 1.19\ kg/m^3$. The airflow is generated by an axial fan linked to a $90\,kW$ synchronous electric motor powered from a computer controlled, variable frequency drive. The test section, located downstream of a $12{:}1$ contraction, has a $3\,m$ streamwise length with a rectangular $1 \times 0.75\,m$ cross-section. At maximum drive, the free stream airflow velocity achieves a value close to $U_e \approx 40\ m/s$, with a characteristic turbulent intensity $Tu_e \approx 0.2\%$. The integration of the SHX within the test section can be selected to best reproduce the key dimensionless parameters characterizing the nominal flight operation, in particular the turbulent boundary layer scales of the approaching flow defined at streamwise location x_i. The SHX/airflow surface is to be placed horizontally across the $0.75\,m$ span of the wind tunnel cross section and along its streamwise length, leading to a 1 m height between the SHX airflow exposed wall and the upper wind tunnel wall, which should establish a negligible streamwise pressure gradient due to boundary layer growth along the SHX extension.

 doi:10.20944/preprints202603.0239.v1

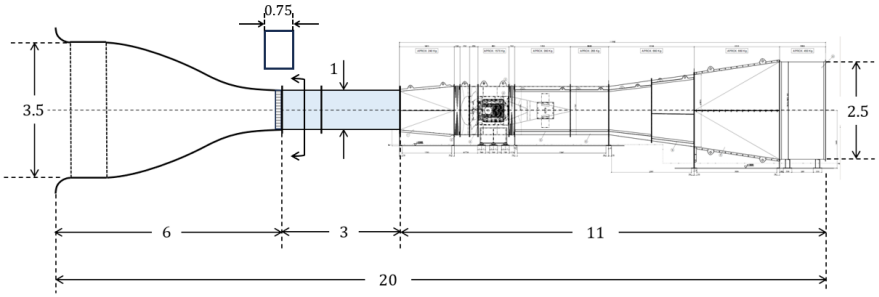

Figure 5. BV4 wind tunnel. Top: general view. Bottom: longitudinal sketch with dimensions in m.

As already mentioned, and according to the dimensional analysis presented in the previous section, physical similarity of the airflow established over the SHX between the flight operation and the wind tunnel scaled tests requires geometrical similarity of the SHX design and matching of the different key dimensionless parameters that appear in expression (18). These include the temperature ratio $\hat{T}_c = T_c/T_e$, and the Reynolds number $Re = \rho_e U_e \Delta_i / \mu(T_c)$. Denoting with subscripts ft, wt respectively the nominal flight and the wind tunnel operations, imposing the matching of these parameters implies:

$$\frac{(T_c/T_e)_{wt}}{(T_c/T_e)_{fl}} \approx 1 \tag{25.1}$$

$$\frac{\Delta_{i,wt}}{\Delta_{i,fl}} \approx \frac{\mu(T_c)_{wt}}{\mu(T_c)_{fl}} \frac{(\rho_e U_e)_{fl}}{(\rho_e U_e)_{wt}} \tag{25.2}$$

Considering $T_{e,wt} \approx 288\,K$ and the nominal flight operation values given in Table 1 fulfilling requirement (25.1) leads to:

$$T_{e,wt} \approx 288\,K \quad \rightarrow \quad T_{c,wt} \approx 389\,K \tag{26}$$

Assuming that the maximum free stream velocity $U_e \approx 40\ m/s$ is used in the wind tunnel tests and with $\mu(T_c)_{ft} \approx 19.5\,\mu Pa \cdot s$, $\mu(T_c)_{wt} \approx 22.7\,\mu Pa \cdot s$, requirement (25.2) for Reynolds number matching establishes the length scale ratio between the two operating conditions:

$$\frac{\Delta_{i,wt}}{\Delta_{i,fl}} \approx 2.01 \tag{27}$$

The above expression indicates that the wind tunnel tests must be performed at a close to 2:1 length scale ratio relative to flight operation mode. Assuming that this scaling ratio is also applied to the sponson and to the SHX solid walls, and that a similar aluminum alloy is used for them in the flight and wind tunnel hardware, the ratio of the streamwise locations selected for the specification of the approaching flow conditions verifies:

$$\frac{\hat{x}_{i,wt}}{\hat{x}_{i,ft}} = \sqrt{\frac{\hat{k}_{w,wt}}{\hat{k}_{w,ft}}} = \sqrt{\frac{\mu(T_c)_{ft}}{\mu(T_c)_{wt}}} \approx 0.93 \tag{28}$$

Expression (28) indicates that the dimensionless position where the approaching flow boundary layer parameters should be matched are very similar in the wind tunnel and in the flight operation. Since the similarity in the boundary layer development establishes matching the values of the dimensionless streamwise coordinate, the dimensionless location to establish the approaching flow conditions for the wind tunnel tests will be approximated as:

$$\frac{\hat{x}_{i,wt}}{\hat{x}_{i,ft}} \approx 1 \quad \rightarrow \quad \hat{x}_{i,wt} \approx -7.5 \tag{29}$$

 doi:10.20944/preprints202603.0239.v1

For the wind tunnel tests, considering the above expression together with the values given in (24) and the 2:1 length scaling ratio found in (27) gives the following specification for the approaching turbulent boundary layer:

$$x_{i,wt} \approx -0.60\ m\text{:}\ \ \Delta_{i,wt} \approx 0.080\ m\,, \quad \frac{u_{\tau,wt}}{U_{e,wt}} \approx 0.038 \tag{30}$$

The location of streamwise station $x_{i,wt}$ should be selected within the test section to give the boundary layer thickness and friction velocity established in expressions (30) for the wind tunnel operating at the selected exterior velocity $U_{e,wt} \approx 40\ m/s$. Figure 6 shows hot-wire measurements conducted within the wind tunnel boundary layer, at the wind tunnel streamwise location $x_{i,wt}$ selected to match the conditions given in (30).

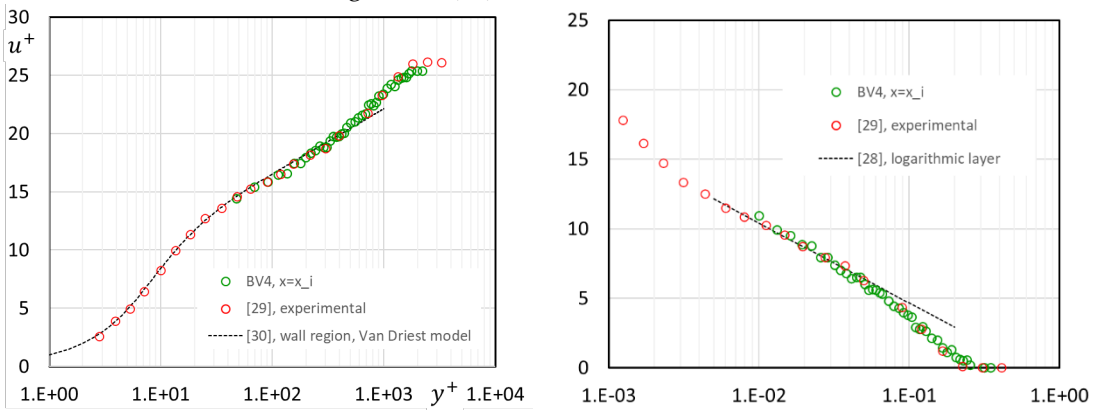

(**a**) (**b**)

Figure 6. Approaching boundary layer velocity profiles for the wind tunnel tests, obtained at the streamwise location verifying (30). **(a)** Wall region scaling. **(b)** Velocity defect region scaling.

The wall region scaling gives the mean velocity and wall distance rendered dimensionless with magnitudes $(u_\tau, \nu_e = \mu(T_e)/\rho_e)$. For the velocity defect region, the scales (u_τ, Δ) are used to construct the dimensionless magnitudes:

$$y^+ = \frac{y u_\tau}{\nu_e},\ \ u^+ = \frac{\bar{u}}{u_\tau}; \qquad \xi = \frac{y}{\Delta},\ \ F = \frac{U_e - \bar{u}}{u_\tau} \tag{31}$$

Expressions (30) provide $Re_{\Delta\tau} \approx 6950$ for the wind tunnel data. The results are compared in Figure 6 to reference ZPG boundary layer data obtained at $Re_{\Delta\tau} \approx 7100$ [29]. This experimental data indicates that the approaching turbulent boundary layer in the wind tunnel compares well with the expected equilibrium profiles characterizing a ZPG turbulent boundary layer of similar development. Furthermore, the resulting turbulent scales obtained from this data provide an almost perfect match to the conditions given in (30). Specifically, the boundary layer scales obtained from the wind tunnel data shown in Figure 5 verify:

$$\Delta_{i,wt} \approx 0.080\ m\,, \quad \frac{u_{\tau,wt}}{U_{e,wt}} \approx 0.039 \tag{32}$$

These results allow positioning the origin of the SHX in the wind tunnel tests that will be consistent with the expected turbulent properties of the airflow approaching the SHX in nominal flight operation.

Assuming that a similar aluminum alloy is used for the sponson and SHX solid walls in both wind tunnel tests and flight hardware, the following values of the dimensionless solid wall thermal conductivity are obtained:

$$\hat{k}_{w,ft} = \frac{k_w Pr}{c_p \mu(T_{c,ft})} \approx 6.1 \cdot 10^3; \quad \hat{k}_{w,wt} = \frac{k_w Pr}{c_p \mu(T_{c,wt})} \approx 5.3 \cdot 10^3 \tag{33}$$

 doi:10.20944/preprints202603.0239.v1

The resulting values of the dimensionless solid walls thermal conductivity are close to each other and both $O(10^3)$. As already discussed, this should ensure a secondary effect of the specific value adopted by the solid wall dimensionless thermal conductivity on the airflow solution.

The imposed physical similarity between the nominal flight operation and the wind tunnel tests implies that similar results should be obtained for dimensionless parameters characterizing the airflow momentum and thermal boundary layers, and thus for the spanwise averaged friction coefficient $c_f(\hat{x})$ and Stanton number $Sta(\hat{x})$:

$$c_f(\hat{x}) = \frac{2\tau_w}{\rho_e U_e^2} \approx \frac{2}{Re\hat{T}_c^n}\left(\hat{h}^n \frac{\partial \hat{u}}{\partial \hat{y}}\right)_{\hat{y}=0} \tag{34.1}$$

$$Sta(\hat{x}) = \frac{q_w}{\rho_e U_e (h_c - h_{ee})} \approx \frac{1}{PrRe(\hat{h}_c - \hat{h}_{ee})\hat{T}_c^n}\left(\hat{h}^n \frac{\partial \hat{h}}{\partial \hat{y}}\right)_{\hat{y}=0} \tag{34.2}$$

The magnitudes τ_w and q_w that appear in the above definitions represent spanwise averaged values, since they are based in dimensionless airflow magnitudes that are also spanwise averaged values. For the definition of the Stanton number, an effective exterior enthalpy h_{ee} is introduced, aimed at partially incorporating back the secondary role played by the exterior airflow Mach number:

$$\hat{h}_{ee} = 1 + a\frac{\gamma - 1}{2}M_e^2, \quad a \approx 1/2 \tag{35}$$

For $a = 0$, the effective exterior enthalpy becomes the static exterior airflow enthalpy h_e. This would be consistent with the approximate boundary layer equations (5) that describe the limit $M_e^2 \to 0$. For $a = 1$, the effective exterior enthalpy becomes the stagnation enthalpy of the exterior airflow, which for an adiabatic ZPG boundary layer would be the proper exterior reference enthalpy to define the Stanton number with non-negligible exterior Mach number effects. The value $a \approx 1/2$ is then taken as a compromise to consider both limits.

Table 2 summarizes the main parameters characterizing the airflow over the SHX for both the nominal flight operation and the wind tunnel scaled tests. The SHX length for the wind tunnels must be compatible with the test section space available in the BV4 wind tunnel, and is chosen as $L_{wt} \approx 1.4\ m$, equivalent to a SHX length for flight operation of $L_{ft} \approx 0.70\ m$.

Table 2. Main parameters characterizing the airflow over the SHX for the nominal flight operation and for the wind tunnel scaled tests.

Parameter	Flight nominal operation	Wind tunnel tests
ISA flight level (hft)	250	21
$p_e\ (kPa)$	37.6	99.0
$\rho_e\ (kg/m^3)$	0.549	1.19
$T_e\ (K)$	239	288
$U_e\ (m/s)$	150	40
$\mu(T_e)\ (\mu Pa \cdot s)$	15.4	18.1
M_e	≈ 0.50	≈ 0.12
SHX cooling fluid	R-1233zd	R-1233zd
$T_c\ (K)$	323	389
T_c/T_e	1.35	1.35
$\mu(T_c)\ (\mu Pa \cdot s)$	19.5	22.7
$\Delta_i\ (m)$	≈ 0.040	≈ 0.080
$u_{\tau i}/U_e$	≈ 0.038	≈ 0.039
Re	≈ 169000	≈ 168000
$x_i\ (m)$	-0.30	-0.60
$L\ (m)$	0.70	1.40
$e_w\ (m)$	0.002	0.004

4. CFD Validation of Wind Tunnel Tests Scaling

Preprints.org (www.preprints.org) | NOT PEER-REVIEWED | Posted: 3 March 2026 doi:10.20944/preprints202603.0239.v1

Numerical validation of the presented wind tunnel tests strategy can be carried out by CFD modeling of the airflow developing over a model of the SHX. A schematic view of the computational domain and boundary conditions used for these numerical studies is shown in Figure 7.

The computational domain includes thermal modeling of the sponson and SHX solid walls. Its inlet is located at the streamwise station $x = x_i$ where the approaching flow Reynolds number Re defined in (15.1) matches both the flight operation and the wind tunnel tests. The temperature distribution in the solid walls is simultaneously solved by assuming an adiabatic boundary condition for the solid walls not exposed to airflow or to cooling fluid, and by setting a prescribed temperature T_c at the cooling fluid channel.

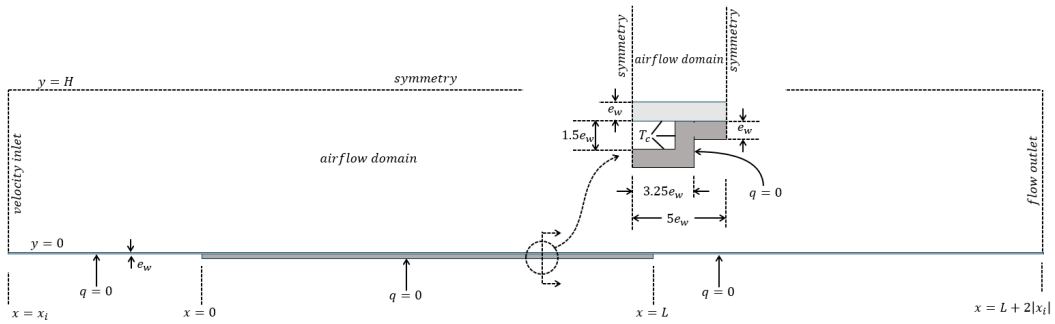

Figure 7. CFD analysis of airflow development over SHX. Computational domain and boundary conditions for airflow and solid wall temperature development over SHX.

Regarding the airflow, velocity inlet conditions including the inlet boundary layer with turbulent magnitudes are prescribed at $x = x_i$. To properly model the inlet boundary layer, an independent numerical simulation is carried out on a ZPG boundary layer, and flow profiles obtained at the downstream station of this simulation that match the inlet boundary layer thickness Δ_i and friction velocity u_τ are taken as inlet boundary condition for the airflow. Symmetry conditions are applied at a cross-stream height $\hat{y} = 6.25$, which matches the mid height of the wind tunnel cross section. Finally, a flow outlet boundary condition is prescribed at $\hat{x} = \hat{L} + 2|\hat{x}_i|$, which is considered sufficient to guarantee a negligible streamwise gradient of the flow.

The numerical simulations were performed using the pressure-based solver of the CFD code Fluent V2025R1 from ANSYS, with and second order discretization and coupled pressure-velocity treatment which allows description of compressibility effects due to the airflow Mach number. The airflow was simulated with air taken as perfect gas. Two similar numerical grids were constructed to define the flight nominal and the wind tunnel test cases. Each numerical grid was developed around hexahedral cells and included clustering to properly resolve the boundary layer and possible streamwise gradients developing at the inlet region of the computational domain. Each resulting grid included a total of $1.1\,MCells$. The normal to wall size of the airflow cell in contact with the wall verifies $\Delta y^+ = \Delta y u_\tau \rho(T_c)/\mu(T_c) = O(1)$, which allows resolving the viscous sublayer within the turbulent boundary layer. Figure 8 shows some views of the numerical grid constructed for the airflow and for the sponson and SHX solid walls. RANS modeling was selected to describe the turbulent flow development, based on the standard $k-\epsilon$ turbulence model using second order discretization of the turbulent fluxes.

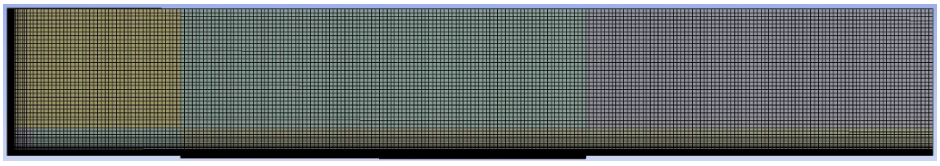

(a)

 doi:10.20944/preprints202603.0239.v1

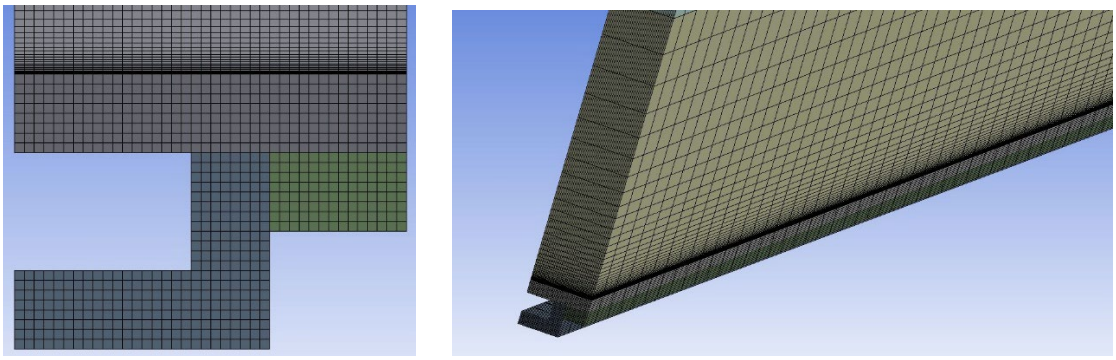

(b) (c)

Figure 8. Details of the numerical grid used in the CFD validation studies. **(a)** Grid cut along the symmetry plane z=0. **(b)** Cross stream cut through the airflow wall region and SHX solid wall. **(c)** 3D view of the airflow near wall region and SHX solid wall.

Figure 9 shows the mean velocity and turbulent profiles applied to the inlet of the computational domain, which reproduce the characteristics of a ZPG boundary layer and verify the turbulent scales set in Table 2 for the approaching boundary layer thickness and friction velocity.

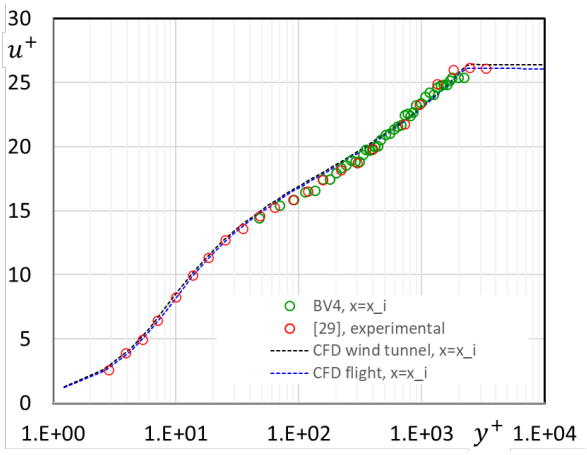

Figure 9. Mean velocity profile applied in the CFD numerical simulations at the inlet of the computational domain, $x = x_i$. CFD inlet profiles for nominal flight and wind tunnel scaled tests simulations compared to wind tunnel experimental data obtained at the downstream coordinate $x = x_i$.

The results of the applied inlet velocity profiles for the CFD simulations of nominal flight and wind tunnel operation are very similar and practically coincide with the experimental data obtained in the assigned streamwise inlet coordinate for the experimental wind tunnel data.

Table 3 summarizes the main characteristics of the boundary layer defined at the inlet streamwise coordinate $\hat{x}_i$, confirming that the Reynolds number is closely matched between the CFD simulations and the experimental wind tunnel data.

Table 3. Main parameters defining the inlet boundary layer for the nominal flight and wind tunnel CFD simulations and for the experimental wind tunnel conditions.

Parameter	Flight CFD	Wind tunnel CFD	Wind tunnel tests
$\Delta_i = \Delta(x_i)\ (m)$	0.040	0.080	0.080
$u_\tau(x_i)\ (m/s)$	5.79	1.52	1.57
$u_\tau/U_e\ (x_i)$	0.039	0.038	0.039
Re	170000	172000	176000

 doi:10.20944/preprints202603.0239.v1

The assumption used in this study of the airflow having a weak spanwise dependence can be checked in Figure 10, showing the spanwise modulation of the dimensionless airflow enthalpy over the SHX solid wall at different downstream locations. The results from the numerical simulations reveal that this modulation is $O(10^{-4})$, thus supporting the simplification introduced in the dimensional analysis presented above, based on averaging the mean airflow magnitudes along the spanwise coordinate.

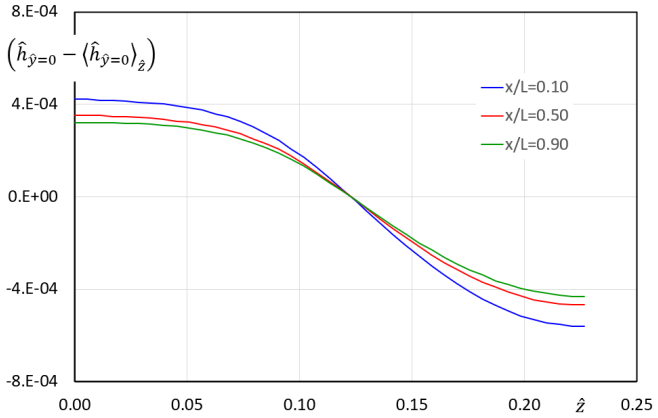

Figure 10. Spanwise modulation of the airflow wall enthalpy for nominal flight operation conditions at different downstream locations.

A comparison of CFD results obtained in the nominal flight and wind tunnel scaled tests environment is presented in Figure 11, showing boundary layer profiles of both dimensionless velocity and enthalpy at coordinates $\hat{x} = 1.75, 8.75, 15.75$ or $\hat{x}/\hat{L} = 0.1, 0.5, 0.9$. A logarithmic scale is used for the wall distance $\hat{y}$ to highlight the wall layer, which defines the friction and heat transfer properties of the boundary layer. The mean velocity exhibits an almost perfect matching for the two different environments in the different downstream locations. Regarding the dimensionless enthalpy, the wall layer shows very similar development in the different downstream locations, although some differences are revealed in the velocity defect region. These differences are expected because of residual effects generated by the external Mach number in the nominal flight environment. Figure 10 also highlights the downstream modification of the enthalpy profile in the velocity defect region, as it becomes progressively heated by the turbulent transport terms.

A confirmation of the global equivalence between the dimensionless airflow evolution for the nominal flight and wind tunnel scale tests environments is presented in Figure 12, showing the downstream evolution of the wall friction coefficient and of the Stanton number defined in expressions (34). As expected from mean velocity results shown in Figure 11 (a), the wall friction coefficient exhibits a remarkable equivalence in both environments. In addition, the definition of an effective exterior enthalpy given in (35) provides a way to compensate for the residual differences in the dimensionless enthalpy that appear in Figure 10. Figure 11 gives also information on the dimensionless relaxation distance $\Delta\hat{x} \sim 5$ that characterizes the heat transfer taking place upstream and downstream of the SHX, due to heating of the sponson wall. This value is compatible with the selected downstream location defined in (30) to establish the approach flow conditions, which require having negligible wall heat transfer effects.

 doi:10.20944/preprints202603.0239.v1

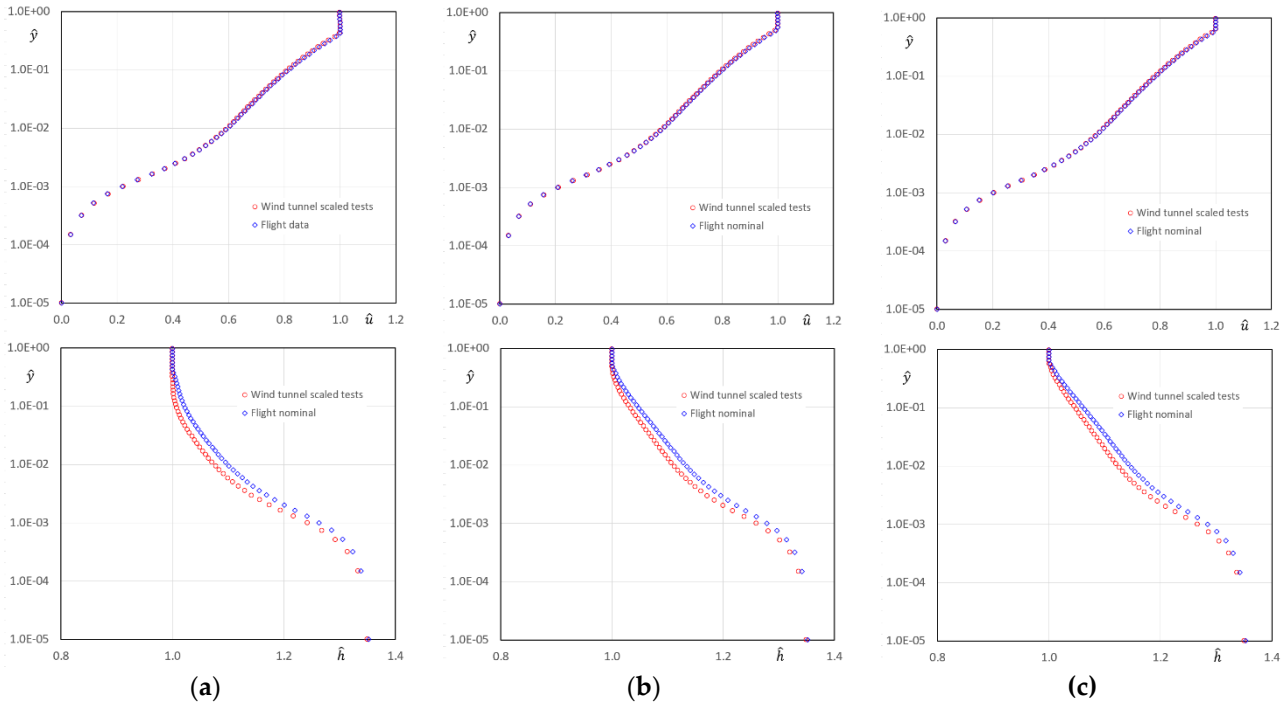

Figure 11. Comparison of CFD results in the airflow boundary layer developing over the SHX for nominal flight and wind tunnel scaled tests environments. Upper row: dimensionless mean velocity profiles. Lower row: dimensionless mean enthalpy profiles. **(a)** $\hat{x}/\hat{L} = 0.1$. **(b)** $\hat{x}/\hat{L} = 0.5$. **(c)** $\hat{x}/\hat{L} = 0.9$.

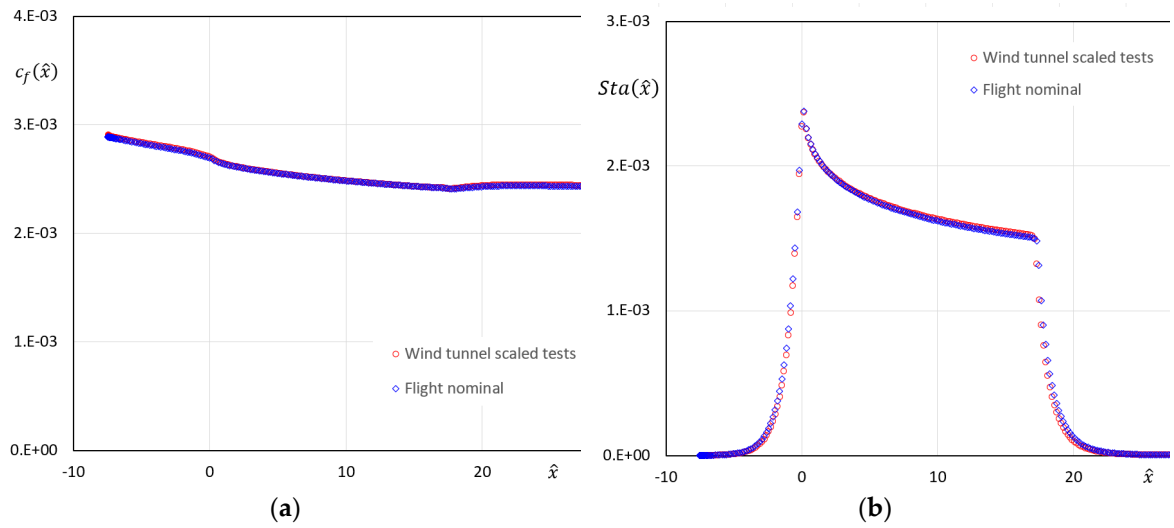

Figure 12. Downstream evolution of the spanwise averaged wall friction coefficient and Stanton number in the SHX boundary layer, showing CFD results from the flight nominal and wind tunnel tests environment. **(a)** Wall friction coefficient. **(b)** Stanton number.

Integrating the data shown in Figure 12 (b) and dividing it by the length of the SHX provides an average value of the Stanton number, which shows a $\sim 0.5\%$ difference between the nominal flight and the wind tunnel scaled tests. Finally, changing the value of the dimensionless solid wall thermal conductivity $\hat{k}_w$ so that both environments share the value defined for the wind tunnel scaled tests leads to a negligible modification of the airflow magnitudes and thus of the SHX wall friction coefficient and Stanton number values. This observation confirms the already suspected secondary role played by this parameter in the evolution of the SHX boundary layer. All the above results seem to indicate the adequacy of the strategy proposed for the wind tunnel scale test program, aimed at providing a good assessment of the expected SHX behavior in the nominal flight operation.

 doi:10.20944/preprints202603.0239.v1

5. Conclusions

Current conceptual studies performed for future HERA applications reveal a significant demand for thermal dissipation which should be ideally met while minimizing aerodynamic, weight, and energy penalties. In this context, SHXs that use the aircraft external airflow as heat sink coupled to phase change cooling circuits provide an attractive means of partially meeting the challenges for heat dissipation. Presently, only conceptual studies have been developed to uncertain the potential of this technology. Increasing the present TRL beyond these studies requires undertaking an experimental test program in a relevant environment, that must strive reproducing the operating conditions to be found in nominal flight operation. For SHX technology this implies reproducing the airflow velocity, pressure, temperature, and wall surface boundary layer development. Alternatively, the technology demonstration can be achieved using wind tunnel facilities operated at near atmospheric conditions provided that physical similarity can be demonstrated between the two operation environments. To this end, the present study has established the secondary role played by the airflow Mach number compared to the airflow heating produced by the temperature ratio established between the SHX wall exposed to the coolant fluid undergoing phase change and the external airflow. The scales involved in the heat transfer problem also show a negligible spanwise modulation of the airflow properties away from local spanwise end effects, which implies that the boundary layer essentially behaves as two-dimensional. Based on these findings, the dimensional analysis of the SHX solid wall/airflow momentum and heat transfer problem allows the identification of the key dimensionless parameters that can render physical similarity between the nominal flight operation and the wind tunnel tests. Specifically, the cooling flow to exterior airflow temperature ratio and the Reynolds number based on the external flow properties and the global boundary layer thickness of the flow approaching the SHX are found to be the two key parameters essentially controlling the flow development. Establishing the Reynolds number equivalence between nominal flight and wind tunnel tests environments leads to fixing the geometrical scale between both operational conditions. Furthermore, it has been demonstrated that additional dimensionless parameters related to the SHX solid wall thermal conductivity play a secondary role in the heat transfer problem, provided that a large enough value of the solid wall thermal conductivity is considered. The proposed wind tunnel scaling tests strategy has been validated by CFD numerical simulations based on RANS turbulence modeling. Introducing the proposed scaling, the numerical simulation results obtained in the nominal flight condition and in the wind tunnel scaled tests demonstrate that both the wall friction coefficient and the Stanton number characterizing the evolution of the heated boundary layer can be closely matched, thus allowing to use the results reduced from the wind tunnel scaled tests to determine the expected SHX response under nominal flight operation conditions. Furthermore, the devised wind tunnel scaled tests strategy also provides hints to analyze the impact of spanwise end effects in the SHX heat transfer process, to properly scale its contribution in the nominal flight environment.

Funding: This research was partially funded by CLEAN AVIATION JOINT UNDERTAKING, grant agreement 101102008 THERMAL MANAGEMENT FOR THE HYBRID ELECTRIC REGIONAL AIRCRAT (TheMa4HERA) under the HORIZONT EUROPE 2.5 CLIMATE ENERGY AND MOBILITY research program (https://cordis.europa.eu/project/id/101102008).

Acknowledgments: The authors greatly acknowledge the support of the TheMa4HERA consortium partners for enabling the publication of this paper. Within this consortium, the authors are especially grateful to the interaction with the colleagues at Airbus Defence and Space-SA for providing the conceptual rendering of the SHX installation in HERA and preliminary data related to the SHX flight operation environment and geometry.

Conflicts of Interest: The authors declare no conflict of interest.

Abbreviations

The following abbreviations are used in this manuscript:

 doi:10.20944/preprints202603.0239.v1

CFD	Computational fluid dynamics
GHG	Green House Gas
HERA	Hybrid electric propulsion regional aircraft
HFO	Hydrofluoroolefin
ICAO	International Civil Aviation Organization
RANS	Reynolds averaged Navier-Stokes equations
SAF	Synthetic aviation fuel
SHX	Surface heat exchanger
SRIA	Strategic Research and Innovation Agenda
TRL	Technology Readiness Level
ZPG	Zero pressure gradient

References

1. Kürten, B.; Cappelletto, M.; Zorgno, M.; Carpino, G,; Magnussøn, A.; Flæten, J.; Areng, M. Sustainable Blue Economy Partnership – Strategic Research and Innovation Agenda **2024**. Available online: https://doi.org/10.5281/zenodo.14243414 (accessed on 9 January 2026).
2. Pettes-Duler, M.; Roboam, X.; Sareni, B. Integrated Optimal Design for Hybrid Electric Powertrain of Future Aircrafts. Energies 2022, 15, 6719, pp. 1-25. https://doi.org/10.3390/en15186719.
3. Coutinho, M.; Afonso, F.; Souza, A.; Bento, D.; Gandolfi, R.; Barbosa, F. R.; Lau, F.; Suleman, A. A Study on Thermal Management Systems for Hybrid–Electric Aircraft. Aerospace 2023, 10, 745, pp. 1-24. https://doi.org/10.3390/aerospace10090745
4. Coutinho, M.; Bento, D.; Souza, A.; Cruz, R.; Afonso, F.; Lau, F.; Suleman, A.; Barbosa, F.R.; Gandolfi, R.; Affonso, W.J.; Odaguil, F.I.K.; Westin, M.F.; dos Reis, R.J.N.; da Silva, C.R.I. A review on the recent developments in thermal management systems for hybrid-electric aircraft. Applied Thermal Engineering 227 (2023) 120427, pp. 1-21. https://doi.org/10.1016/j.applthermaleng.2023.120427
5. Broatch, A.; Olmeda, P.; García-Tíscar, J.; Felgueroso, A.; Chávez-Modena, M.; González, L.M.; Gelain, M.; Couilleaux A. Experimental aerothermal characterization of surface air-cooled oil coolers for turbofan engines. International Journal of Heat and Mass Transfer 190 (2022) 122775. https://doi.org/10.1016/j.ijheatmasstransfer.2022.122775
6. Broatcha, A.; García-Tíscar, J.; Felgueroso, A.; Chávez-Modena, M.; González, L.M.; Valero E. Numerical and experimental analysis of rounded fins for high speed air-cooled heat exchangers. International Journal of Heat and Mass Transfer 201 (2023) 123575. https://doi.org/10.1016/j.ijheatmasstransfer.2022.123575
7. Afonso, F.; Sohst, M.; Diogo, C.M.A.; Rodrigues, S.S.; Ferreira, A.; Ribeiro, I.; Marques, R.; Rego, F.F.C.; Sohouli, A.; Portugal-Pereira, J.; Policarpo, H.; Soares, B.; Ferreira, B.; Fernandes, E.C.; Lau, F.; Suleman, A. Strategies towards a more sustainable aviation: A systematic review. Progress in Aerospace Sciences 137 (2023) 100878. https://doi.org/10.1016/j.paerosci.2022.100878
8. Kellermann, H.; Habermann, A.L.; Hornung, M. Assessment of Aircraft Surface Heat Exchanger Potential. Aerospace 2020, 7, 1, pp. 1-19. https://doi.org/10.3390/aerospace7010001
9. Haaland, S.E. Simple and Explicit Formulas for the Friction Factor in Turbulent Pipe Flow. J. Fluids Eng. 1983, 105, pp. 89-90. https://doi.org/10.1115/1.3240948
10. Incropera, F.P.; DeWitt, D.P.; Bergman, T.L.; Lavine, A.S. Principles of Heat and Mass Transfer, 7th ed.; International Student Version; Wiley: Singapore, 2013
11. Schultz-Grunow, F. New frictional resistance law for smooth plates. Luftfahrtforschung Vol. 17, nº 8, 1940, 239–246. https://digital.library.unt.edu/ark:/67531/metadc63129/m2/1/high_res_d/19930094430.pdf (accessed on 30 January 2026)
12. Schlichting, H.; Gersten, K. Boundary-Layer Theory; Springer: Berlin/Heidelberg, Germany, 2017
13. Abreu, R.; Santos, P.; Afonso, F.; Suleman, A. A study on the potential of skin heat exchangers for hybrid-electric aircraft. Applied Thermal Engineering 280 (2025) 128096, pp. 1-13. https://doi.org/10.1016/j.applthermaleng.2025.128096
14. Kallath, H.; Kholi, F.K.; Ha, M.Y.; Min, K.J.; Chetwynd-Chatwin J. Computational Study on the Aerodynamics of a Surface-Heated Wing for Thermal Management. AIAA JOURNAL Vol. 58, No. 10, October 2020, pp. 4339-4356. https://doi.org/10.2514/1.J059220

 doi:10.20944/preprints202603.0239.v1

15. Habermann, A.L.; Khot, A.; Lampl, D.E.; Perren, C. Aerodynamic Effects of a Wing Surface Heat Exchanger. Aerospace 2023, 10, 407, pp. 1-25. https://doi.org/10.3390/aerospace10050407
16. Li, B.; Sun, Q.; Xiao, D.; Zhang, W.; Numerical Investigation of the Aerofoil Aerodynamics with Surface Heating for Anti-Icing. Aerospace 2022, 9, 338. https://doi.org/10.3390/aerospace9070338
17. Menter, F.R.. Two-equation eddy-viscosity turbulence models for engineering applications, AIAA J. 32 (8) (1994) 1598–1605, http://dx.doi.org/10.2514/3.12149
18. Spalart, P.R.; Allmaras, SR.. A one-equation turbulence model for aerodynamic flows, in: 30th Aerospace Sciences Meeting and Exhibit, Reno, NV, USA, 1992, http://dx.doi.org/10.2514/6.1992-439.
19. Poinsatte, P.E. Heat Transfer Measurements From a NACA 0012 Airfoil in Flight and in the NASA Lewis Icing Research Tunnel. NASA Contractor Report 4278, 1990. https://ntrs.nasa.gov/api/citations/19900009887/downloads/19900009887.pdf (accessed on 28 January 2026).
20. Felgueroso, A.; González-Nieves, I.; Díaz-Barja, M.; García-Rodríguez, J. Numerical modeling of a two-phase Skin Heat Exchanger for Hybrid-Electric Regional Aircraft. AIAA Aviation Forum and ASCEND, No. 2024-3579, 2024.
21. Chaquet, J.M.; Torres, G. Efficient Phase-Change Fluid Model Applied to a Skin Heat Exchanger 3D Steady Thermal Simulation. TSAS2025: "Towards Sustainable Aviation" Summit. Toulouse, France, January 28-30, 2025.
22. Shah, M.M. A General Correlation for Heat Transfer during Flow Condensation inside Pipes. Heat and Mass Transfer, 1979, pp. 547–556. https://doi.org/10.1016/0017-9310(79)90058-9
23. Torres, G; Chaquet, J.M.; Jauntsarats, O.; Carrasco, D. Thermo-Mechanical Simulation of a Skin Heat Exchanger Considering Phase-Change Thermal Boundary Conditions. Proceedings of ASME Turbo Expo 2025, Turbomachinery Technical Conference and Exposition. GT2025-15667. June 16-20, 2025, Memphis, Tennessee, USA. https://doi.org/10.1115/GT2025-151667
24. Schaefer, S.; Quaium, F.; Muhsal, N.; Speerforck, A.; Thieleck, F.; Becker, C. Integration of a Cooling System Architecture with a Skin Heat Exchanger for High Thermal Loads in Fuel Cell Powered Aircraft. 19th International Refrigeration and Air Conditioning Conference at Purdue, USA, July 10-14, 2022. https://docs.lib.purdue.edu/iracc/2347/ (accessed on 30 January 2026)
25. Cebeci, T; Bradshaw, P. Physical and Computational Aspects of Convective Heat Transfer, Springer-Verlag (1988) https://doi.org/10.1007/978-1-4612-3918-5.
26. Pirozzoli, S; Smits, A.J. Outer-layer universality of the mean velocity profile in turbulent wall-bounded flows. Phys. Rev. Fluids 8, 064067, June 2023 https://doi.org/10.1103/PhysRevFluids.8.064607.
27. Wilcox, D.C. Turbulence Modeling for CFD. DCW Industries (2006), ISBN 978-1928729082.
28. Tennekes, H.; Lumley, J.L. A First Course in Turbulence. MIT Press (2018), ISBN 978-0262536301.
29. DeGraaff, D.B.; Eaton, J.K. Reynolds-number scaling of the flat-plate turbulent boundary layer. J. Fluid Mech. 422, pp. 319-346 (2000).
30. Pope, S.P. Turbulent Flows. Cambridge University Press (2000), ISBN 13: 9780521598866.